Journal Pre-proof

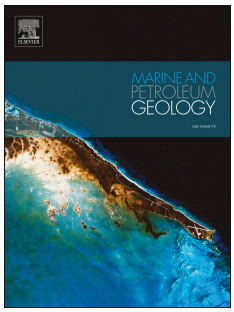

Analysis of marine controlled source electromagnetic data for the assessment of gas hydrates in the Danube deep-sea fan, Black Sea

Katrin Schwalenberg, Romina A.S. Gehrmann, Jörg Bialas, Dennis Rippe

PII: S0264-8172(20)30433-5

DOI: https://doi.org/10.1016/j.marpetgeo.2020.104650

Reference: JMPG 104650

To appear in: *Marine and Petroleum Geology*

Received Date: 4 November 2019

Revised Date: 23 July 2020

Accepted Date: 7 August 2020

Please cite this article as: Schwalenberg, K., Gehrmann, R.A.S., Bialas, Jö., Rippe, D., Analysis of marine controlled source electromagnetic data for the assessment of gas hydrates in the Danube deep-sea fan, Black Sea, *Marine and Petroleum Geology* (2020), doi: https://doi.org/10.1016/j.marpetgeo.2020.104650.

This is a PDF file of an article that has undergone enhancements after acceptance, such as the addition of a cover page and metadata, and formatting for readability, but it is not yet the definitive version of record. This version will undergo additional copyediting, typesetting and review before it is published in its final form, but we are providing this version to give early visibility of the article. Please note that, during the production process, errors may be discovered which could affect the content, and all legal disclaimers that apply to the journal pertain.

© 2020 Published by Elsevier Ltd.

Journal Pre-proof

Credit Author Statement

Katrin Schwalenberg:	Conceptualization, Methodology, Validation, Investigation, writing – Original Draft – Review & Editing, Visualization, Supervision, Project Administration
Romina Gehrmann:	Conceptualization, Methodology, Software, Validation, Writing - Review & Editing
Jörg Bialas:	Validation, Investigation, Writing - Review & Editing, Supervision, Project Administration
Dennis Rippe:	Investigation, Data Curation, Writing - Review & Editing

Journal Pre-proof

Journal Pre-proof

Analysis of marine controlled source electromagnetic data for the assessment of gas hydrates in the Danube deep-sea fan, Black Sea

Katrin Schwalenberg[1], Romina A.S. Gehrmann[2], Jörg Bialas[3], Dennis Rippe[4]

[1] BGR Federal Institute for Geosciences and Natural Resources, Hanover, Germany

[2] University of Southampton, Ocean and Earth Sciences, National Oceanography Centre Southampton, Southampton, UK

[3] GEOMAR Helmholtz Centre for Ocean Research Kiel, Germany

[4] Helmholtz Centre Potsdam, GFZ German Research Centre for Geosciences, Potsdam, Germany

Journal Pre-proof

Abstract

Marine controlled source electromagnetic (CSEM) data have been analyzed as part of a larger interdisciplinary field study to reveal the distribution and concentration of gas hydrates and free gas in two working areas (WAs) in the offshore Danube fan in the western Black Sea. The areas are located in the Bulgarian sector in about 1500 m water depth (WA1) and in the Romanian sector in about 650 m water depth (WA2). Both areas are characterized by channel levee systems and wide spread occurrences of multiple bottom simulating reflections (BSRs) suggesting the presence of gas hydrates. Electrical resistivity models have been derived from two-dimensional (2D) inversions of inline CSEM data using a seafloor-towed electric dipole-dipole system. Comparing the resistivity models with coincident reflection seismic profiles reveals insight in the sediment stratigraphy of the gas hydrate stability zone (GHSZ). Gas hydrate and free gas saturation estimates have been derived with a stochastic approach of Archie's relationship considering uncertainties in the input parameters available from drilling with the MeBo-200 seafloor rig in WA2.

The resistivity models generally reflect the transition of marine to lacustrine conditions expressed by a sharp decay of pore water salinities in the top 30-40 m below seafloor caused by freshwater phases of the

Journal Pre-proof

Black Sea due to sea level low stands in the past. In WA1, we derived saturation estimates of 10-20% within a 100 m thick layer at around 50 m depth below the channel which compares well with estimates from seismic P-wave velocities. The layer extends below the western levee with even higher saturations of 20-30%, but high gas hydrate saturations are unlikely within the fine grained, clayey sediment section, and the high resistivities may reflect different lithologies of lower permeability and porosity. The resistive layer terminates below the eastern levee where increasing resistivities at depth towards a stack of multiple BSRs indicate gas hydrate and free gas concentrations in the order of 10% to locally 30%. WA2 is characterized by a major slope failure at the landward edge of the gas hydrate stability field next to the channel. Gas hydrate saturation estimates within the slump area are close to zero within the GHSZ which is in agreement with coring results of the nearby MeBo drill sites. Elevated resistivities below the steeply upward bending BSR lead to saturation estimates less than 10% of free gas that may have accumulated.

Keywords: gas hydrate assessment; marine controlled source electromagnetics; 2D inversion; western Black Sea

Journal Pre-proof

Journal Pre-proof

1. Introduction

The electrical resistivity derived from marine controlled source electromagnetic (CSEM) data can be related to the presence and volumes of gas hydrates in sub-seafloor sediments (Edwards, 1997). Gas hydrates are stable at high pressure and low temperature. These conditions are found around the globe in marine sediments along most continental margins, in permafrost grounds, and deep lakes (e.g. Sloan and Koh, 2007). The interest in gas hydrate research is attributed to the large amount of methane stored in hydrates globally. Yet, estimates of the global gas hydrate inventory differ by orders of magnitude between ~500 and 56,000 gigatons of carbon (e.g Boswell and Collett, 2011; Milkov 2004; Piñero et al., 2013; Ruppel and Kessler 2017; and references therein).

Gas hydrate deposits have been commonly identified in reflection seismic data by imaging bottom simulating reflections (BSRs) originating in most cases from a layer of free gas beneath the base of the gas hydrate stability zone (GHSZ) and solid gas hydrates filling the pore space above causing a seismic impedance contrast (e.g. Hyndman and Spence, 1992). While reflection seismic data provide relevant structural information, the observation of a BSR is not a significant measure for how much gas hydrate may have formed within the GHSZ. Gas hydrates are also known to exist without a BSR (Sloan and Koh, 2007; Majumdar et al., 2016). Other indicators for seismically derived gas hydrate accumulations can be locally observed high-amplitude reflections and blank zones caused by dispersed gas hydrates scattering seismic energy. Free gas may penetrate into the GHSZ along fluid conduits such as geological faults and chimneys, possibly forming gas hydrate sweet spots within the GHSZ (e.g. Riedel et al., 2006). Seafloor vents may occur when these conduits reach the seafloor where they can be identified using hydro-acoustic methods (Vassilev, 2005; Naudts et al., 2006; Riboulot et al., 2017). Only a few percent of gas hydrate or free gas in the sediment may cause amplitude anomalies and blanking, making it difficult to account for high saturation reservoirs from reflection seismic data alone. Seismic velocities are generally higher where gas hydrates have formed in the sediment matrix, and lower in free gas zones (e.g. Andreassen et al., 1997).

Marine CSEM methods offer the opportunity to provide area-wide volume estimates of gas hydrate and free gas saturations. Gas hydrates are electrically resistive and form in the pore space, which is typically filled with conductive, i.e. saline pore fluid (Edwards, 1997; Spangenberg, 2001). Thus, the presence of gas

hydrates increases the formation or bulk resistivity of a sediment section. Free gas also increases the formation resistivity. It is therefore difficult to distinguish between free gas and gas hydrates from CSEM data alone. The combination of electrical resistivity information from CSEM with seismic reflection and velocity data has demonstrated to constrain structure, differentiate between free gas and gas hydrate, and to provide more accurate saturation estimates (e.g. Goswami et al., 2015; Weitemeyer et al., 2017; Schwalenberg et al., 2017; Bialas et al., 2020, this issue). Ground truthing is still required from coring and drilling (e.g. Tréhu et al., 2006; Expedition 311 Scientists, 2006).

We report on the analysis and interpretation of two-dimensional (2D) marine CSEM data collected in two working areas (WAs) in the offshore Danube fan, western Black Sea. The data were acquired during R/V Maria S. MERIAN cruise MSM35 in early 2014 (Schwalenberg et al., 2014) with the goal to identify and evaluate possible gas hydrate targets. Time domain CSEM data along three profiles have been interpreted in terms of resistivity models using state-of-the-art 2D inversion (Key, 2016). We compare the resistivity models with coincident reflection seismic profiles and seismic velocity information. Gas hydrate saturation estimates have been calculated applying a stochastic approach of Archie's relationship (Archie, 1942) after Sava and Hardage (2007) using porosity, salinity and resistivity data from MeBo drilling (Bohrmann et al., 2018, Riedel et al., 2020, this issue).

2. Geology of the Western Black Sea

The Black Sea is a quasi-closed marginal sea formed during the Lower Cretaceous with unusually thick sediments in the basins. Anoxic conditions have favored the production of methane (Reeburgh et al., 1991), and the formation of gas hydrates within the stability field (Kessler et al., 2006). During the last glacial maximum, about 20 k years ago, most of the shelf regions have been exposed leading to high seafloor temperatures of 9°C (Soulet et al., 2010) and extended fresh water phases which have not equilibrated today (Degens and Ross, 1974). Present pore water salinities decay from 22 psu (practical salinity units) at the sea-bottom (Murray et al., 1991) to values between 1 and 4 psu measured on core samples down to 30 m below seafloor (mbsf) at the outer edge of gas hydrate stability of the Danube fan (Ker et al., 2019) and within the GHSZ down to 144 mbsf using the MeBo-200 drill rig (Bohrmann et al., 2018).

Journal Pre-proof

Large parts of the continental slopes lie within the gas hydrate stability field which extends seawards from water depths exceeding 620 - 725 m (Vassilev and Dimitrov, 2002; Lüdmann et al., 2004; Popescu et al., 2007). The presence of gas hydrate has been inferred from direct sampling (Vassilev and Dimitrov, 2002; Riboulot et al., 2018), seismic data mapping the BSR (Lüdmann et al., 2004; Popescu et al., 2006; Baristeas, 2006; Zander et al., 2017; Minshull et al., 2019), and degassing experiments of sediment samples (Heeschen et al., 2011; Pape et al., 2011). Strong methane seepage from the seafloor has been reported from almost everywhere along the continental margins of the Black Sea (Vassilev and Dimitrov, 2002; Naudts et al., 2006; Klaucke et al., 2006; Schmale et al., 2011; Riboulot et al., 2017), and from mud volcanism in the deeper parts (Kruglyakova et al., 2004; Greinert et al., 2006).

2.1 Working Areas

The Danube fan in the western Black Sea offshore Bulgaria and Romania has been the focus area of field studies within the German SUGAR project (Haeckel et al., 2015; Wallmann and Bialas, 2009; Figure 1a). Two WAs were chosen for more detailed geophysical investigations during R/V MERIAN cruises MSM34 and MSM35 including high resolution 2D and 3D seismic data (P-cable), ocean bottom seismometer (OBS) data and heat flow (Bialas et al., 2014), as well as 2D and 3D controlled source electromagnetic data sets (Schwalenberg et al., 2014). WA1 is located in the Bulgarian sector in water depths around 1500 m and includes one of the older channel levee systems of the Danube fan referred to as S1 channel in the following (Figure 1b). It is characterized by stratified levee sediments, mass transport deposits and several buried paleo channels (Zander et al., 2017). A stack of four BSRs is imaged within the channel (Popescu et al., 2006; Baristeas, 2006). The shallowest BSR at depths of about 320 - 380 mbsf indicates the recent base of gas hydrate stability (Zander et al., 2017). A high P-wave velocity zone derived from OBS data has been modeled at intermediate depth below the S1 channel, possibly indicating a layer of low saturation pore filling gas hydrates based on the absence of shear wave anomalies. Seismic velocities further increase with depth towards the recent BSR and drop just below the BSR likely due to the free gas layer below (Bialas et al., 2020, this issue). WA1 has no indication of vertical fluid flow and gas migration through the GHSZ. In this study we analyze two CSEM lines with profile P1 covering the S1 channel and parts of the western and

Journal Pre-proof

eastern levees coincident to multi-channel seismic line 1107, and profile P2 covering the S1 channel towards the eastern levee (see Figure 1b). Analysis of a 3D CSEM data set across the S1 channel is subject to Duan et al. (this issue).

WA2 is located in the Romanian sector in water depths between 500 and 800 m at the landward edge of the GHSZ next to the S2 canyon of the offshore Danube fan (Figure 1c). It is characterized by a major slope failure referred to as the S2 slump area and an anomalously upward bending BSR. Gas migration and gas flares are abundant in the vicinity of the S2 canyon at water depths of less than 700 m outside the GHSZ (Hillman et al., 2018) and further up the slope (Soulet et al., 2010; Riboulot et al., 2018). MeBo drilling was carried out at coincident sites 17 and 19 located near the S2 slump area (Bohrmann et al., 2018; Figure 1c) Site MeBo-17 reached the BSR at 144 mbsf, but no direct evidence of gas hydrate has been found in any of the MeBo drill sites (Bohrmann et al., 2018, Riedel et al., 2020, this issue). In WA2 we analyze and interpret data of one CSEM line (profile P3) across the S2 slump area.

Journal Pre-proof

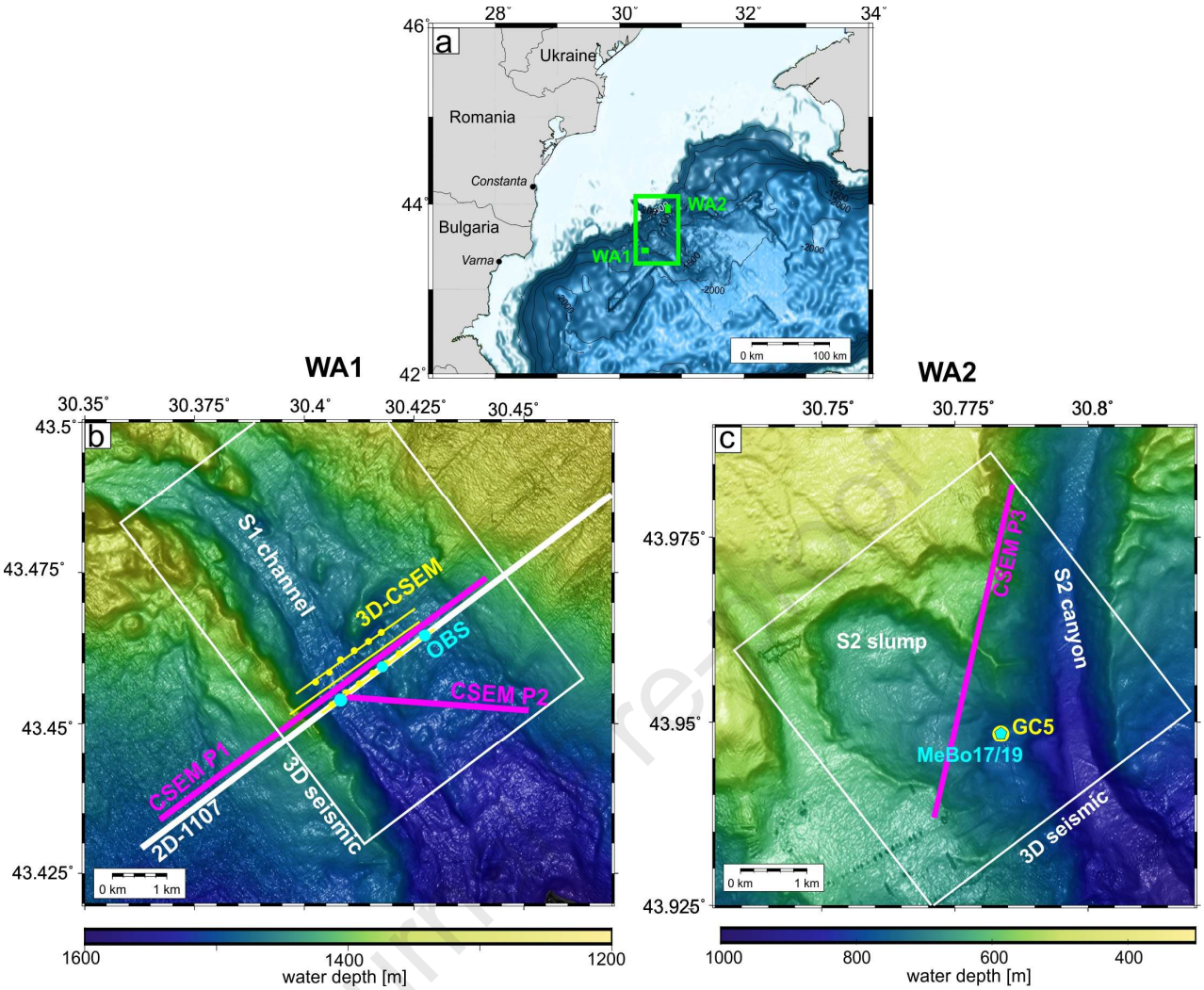

Figure 1: a) Overview map of the western Black Sea showing the location of the working areas. b) Bathymetry of working area 1 in the Bulgarian Sector in water depth around 1500 m across the S1 channel. Purple lines: CSEM profiles P1 and P2 analyzed in this paper, white lines: 2D seismic line 1107 and outline of the 3D seismic cube, light blue dots: location of ocean bottom seismometer, yellow lines and dots: 3D CSEM data set analyzed in Duan et al, (this issue). c) Working area 2 in the Romanian Sector in water depths between 500 to 800 m at the landward edge of gas hydrate stability. Purple lines: CSEM profile P3 analyzed in this paper. White line: outline of 3D seismic cube, yellow dot: location of gravity core 5, light blue dot: location of MeBo sites 17 and 19.

3. Materials and Methods

3.1 CSEM Instrumentation

We used a seafloor-towed electric dipole-dipole system (HYDRA) to collect 2D time domain CSEM data. The system consists of a heavy instrument platform called “pig”, a 108 m long transmitting dipole (TX) and up to five receiving dipoles (RX) of lengths between 15 m and 20 m connected in-line at offsets from 150 m to 850 m behind the TX (Figure 2). The system is modular which means receiving units can be added or removed from the array, and offsets can be varied in order to adapt to seafloor conditions and target depths. The pig keeps the array on the seafloor while towing, and contains the telemetry unit, the CSEM transmitter, a conductivity – temperature – depth (CTD) - probe, and an acoustic ultra-short baseline (USBL) transponder. Each receiving dipole is connected to a data logger with low-noise front end electronics, sampling the inline component of the ambient electric fields at 10 kHz.

The HYDRA system has been modified from previous surveys (Gehrmann et al., 2015; Schwalenberg et al., 2017): i) For the first time a newly developed deep-sea CSEM transmitter was used which is mounted inside the pig, powered by a 500 V onboard power unit and capable to transmit current signals of up to 20 A in amplitude. The new transmitter was used at profile P2, but due to technical problems replaced with a backup current transmitter placed in the lab onboard the vessel at profiles P1 and P3. ii) A new telemetry unit was also installed inside the pig, and enabled online communication and data transfer between the onboard and seafloor units via the opto-electrical deep-tow cable. iii) Two receiver units were newly developed to allow online communication and data transfer via Ethernet connection to the telemetry unit inside the pig. Thus, quality checks of the data have become possible during deployments. Transmitter and receiver units communicate with the telemetry unit via fast DSL-modems. Up to three autonomous, otherwise identical receiver units described in Gehrmann et al. (2018) are connected by rope und towed behind. CSEM transmitter and all RX receiver units are equipped with a high precision atomic clock which were synchronized prior to each deployment.

We applied a continuous square wave source signal with a period of 6 s and +/- 15 A amplitude which was reduced to +/- 10 A in case of the backup current transmitter (see data examples in the Supplementary Materials).

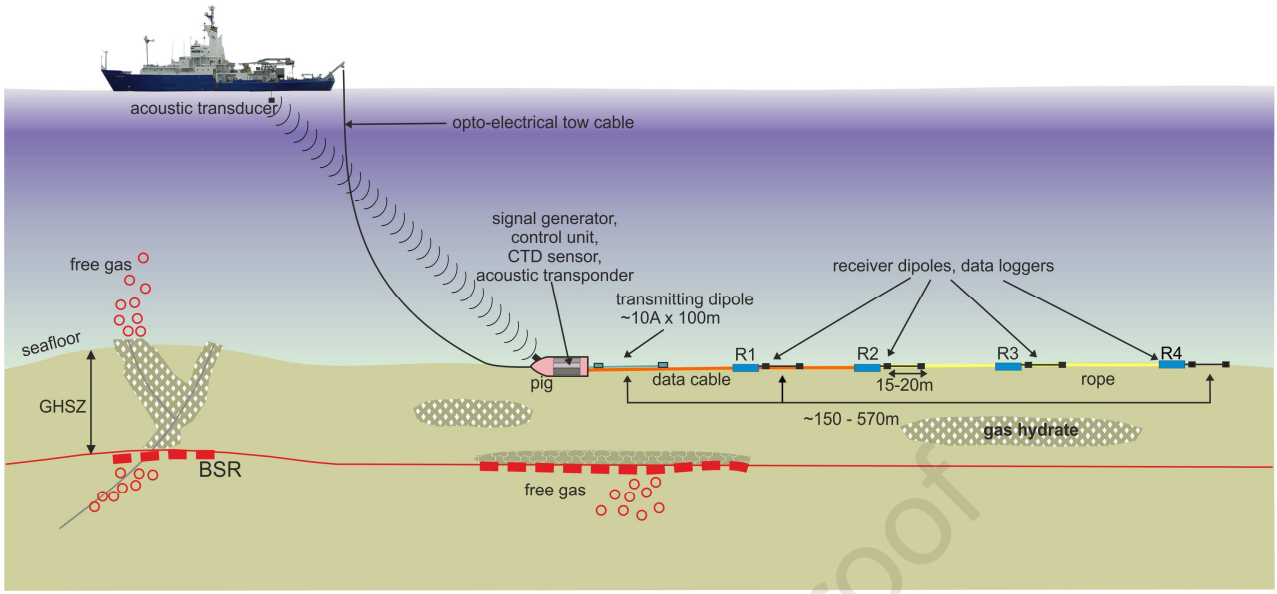

Figure 2: Set-up of BGR's seafloor-towed electric dipole-dipole system HYDRA.

3.2 CSEM Surveying

For surveying, HYDRA was aligned on the seafloor and towed behind the ship at a low speed around 1 knot with a cable length of about three-times the water depth being paid out. The seafloor array was kept stationary for about 5 minutes every 300 m and 150 m across the S1 channel in WA1 to collect clean time series data, but data were also recorded during transits between sites referred to as "roll-on" data. Survey progress was monitored by displaying the USBL transponder coordinates of the pig on a calibrated map in the control lab onboard. Profile directions were chosen with priority to match with seismic lines, but were subject to wind and wave directions.

3.3 CSEM Data Processing

Data processing of the CSEM data sets included gain and drift corrections, and selection of time intervals while HYDRA was stationary at each site. A mean stack and standard deviation is calculated from individual half periods of each receiver and the transmitter within the time intervals discarding outliers that would bias the stack. Roll-on data, recorded while the array was slowly towed on the seafloor, are included in the inversion of profile P1, but were not used in the inversion of profiles P2 and P3 due to high noise

Journal Pre-proof

194 levels.

195 In the frequency domain, the individual periods of all receivers and the transmitter signals at each site are
196 transferred using fast Fourier transform. Real and imaginary parts of the earth response are calculated at
197 eight logarithmically spaced frequencies in the range of 0.167 to 300 Hz for profile P1 and 0.167 to 55.5 Hz
198 for profiles P2 and P3 from stacked auto and cross correlations using relative and absolute error estimates
199 (see Supporting Information in Schwalenberg et al., 2017, and Appendix in Gehrmann et al., 2018 for
200 further details). Additional error floors of 1%, 2% and 3% were added to the data of receivers R1, R2, and
201 R4, respectively, to facilitate convergence of the inversion process.

202

203 *3.4 CSEM Data*

204 Even though we managed to tow up to five receiver units and dipoles behind the TX with a maximum
205 length of 900 m of the seafloor array, not all receivers recorded useful data due to operating errors and
206 mechanical problems with the moulds and connectors of the receiver cables. The data we finally used for
207 the inversion are of high quality as demonstrated by the time series examples in the Supplementary
208 Materials. Table 1 gives an overview which data and offsets have been used in the inversions of the
209 respective profiles.

210

211 *Table 1: Overview or receivers, offsets, number of sites used in the 2D inversions and number of iterations*
212 *to reach the target misfit for the profiles shown in Figures 3, 4, and 5.*

Profile	**P1 / WA1**	**P2 / WA1**	**P3 / WA2**
Receiver Offsets	R1: 153 m R2: 259 m R4: 572 m	R1: 153 m R3: 359 m (8 sites) R4: 560 m (13 sites)	R1: 153 m R2: 259 m
# Sites	32 (+140 roll-on)	14	19
Frequency Range / # No.	0.167 – 300 Hz #8	0.167 – 55.5 Hz #8	0.167 – 55.5 Hz #8
# Iterations	10	7	6

RMS	1.30	1.00	1.00
Figure	3	4	5

213

214

215 *3.5 Electrical Resistivity and Gas Hydrate Saturation*

216 The electrical resistivity of the sub-seafloor derived from CSEM data depends on the sediment porosity,
217 and the salinity and temperature of the pore fluid. In the presence of gas hydrates as well as free gas, the
218 formation resistivity increases, as both gas hydrate and free gas are electrically resistive replacing
219 conductive pore water in the sediments. The well-known empirical Archie relationship (Archie, 1942) is
220 typically used to derive estimates of the gas hydrate or free gas saturation from electrical resistivity data. Its
221 general form can be written as

222 $$\rho_0 = a\,\rho_\omega\,\phi^{-m} \quad (1)$$

223 with ρ_0: formation resistivity of hydrate-free or gas-free sediments, ρ_ω: pore fluid resistivity, ϕ: porosity ,
224 and the empirical and dimensionless Archie coefficients *a* and cementation factor *m.* If gas hydrate, free gas
225 or another constituent are present, Archie's relationship can be extended to

226 $$\rho_f = a\,\rho_\omega\,\phi^{-m}\,S_\omega^{-n} \quad (2)$$

227 where ρ_f: formation resistivity of sediment containing hydrate or free gas, S_ω: pore water saturation, and *n*:
228 empirical saturation exponent. The gas hydrate or free gas saturation S_{gh} = (1- S_ω) can then be calculated
229 using

230 $$S_{gh} = 1 - \left(a\,\rho_\omega \Big/ \phi^m\,\rho_f \right)^{1/n} \quad (3)$$

231 Note, eq. 2 demonstrates that the gas hydrate / free gas saturation becomes independent of the pore water
232 properties and porosity, if a valid background resistivity model can be found. In that case it is

233 $\rho_f = \rho_0\,S_\omega^{-n}$ and

$$S_{gh} = 1 - \left(\rho_0 / \rho_f\right)^{1/n} \quad (4)$$

The choice of Archie coefficients *a* and *m* has been widely discussed in the literature, and has been derived for a wide range of artificial and natural samples including various sediment types whereby *m* generally increases as the sediment particles become less spherical (e.g. Archie, 1942; Jackson et al., 1978). Salem and Chilingarian (1999) renamed *m* shape factor and found that *m* varies between 1.2 and 3.0 for a wide range of heterogeneous and compacted lithologies with variable grain and pore sizes and shapes. The parameter *a* was introduced by Winsauer et al. (1952) to allow a better fit to the sample data, but is theoretically 1.0 as the formation factor $F = \rho_f / \rho_w$ should be 1.0 at 100% porosity. Practically, *a* and *m* are derived from core samples of hydrate-free or gas-free background sediments where *m* is the slope of the formation factor - porosity – relationship, and *a* is the intercept at 100% porosity (e.g. Salem and Chilingarian, 1999; Collett and Ladd, 2000; Riedel et al., 2020, this issue).

The saturation exponent *n* has been estimated experimentally and theoretically. Pearson et al. (1983) derived an average value of *n* = 1.9386 for frozen permafrost samples as an analog for gas hydrate filled sediments. Spangenberg (2001) used a range of hydrate bearing network models and found saturation factors between 0.5 and 4, with larger *n* for reduced pore space connectivity, and further points out that the saturation factor clearly depends on the cementation factor *m*, the porosity, mean grain size and distribution, and the saturation itself. Cook and Waite (2018) recently suggested to use a saturation factor of *n=2.5 +/- 0.5* for gas hydrate settings in the absence of independent estimates.

It therefore seems unlikely that the same set of Archie coefficients may apply to the different sediment types in the Black Sea working areas. However, based on the MeBo drilling data in WA2 we can provide a parameter range and dependency for *a* and *m*, and estimate a range for *n*.

The presence of clay also strongly affects the formation resistivity and Archie coefficients, and may lead to false saturation estimates, if it remains unconsidered (e.g. Worthington, 1993). Generally, due to its shape clay affects the tortuosity of the pore space, and is mostly reflected in *m* which typically increases as the clay content increases (Jackson et al., 1978; Salem and Chilingarian, 1999).Various models have been

suggested to account for the conductivity of clay (shaly sand correction). Lee and Collett (2006) make use of the shaly sand model by Simandoux (1963) where the conductivity of the clay minerals is added to the formation conductivity. The gas hydrate saturation for shaly sands can then be written as

$$S_{gh} = 1 - \left(a\,\rho_\omega \left(1 - \rho_f\, Q_c\right) \Big/ \phi^m\, \rho_f \right)^{1/n} \quad . \tag{5}$$

where $Q_c = {V_c(1-\phi)}/{R_c}$ is the effective clay conductivity, V_c the volume fraction of clay in the solid matrix and R_c the resistivity of clay (Lee and Collett, 2006).

3.6 Stochastic Determination of Gas Hydrate Saturations

In order to calculate saturation estimates from the resistivity models, we apply stochastic simulations of Archie's relationship following the procedure suggested by Sava and Hardage (2007). The input parameters are represented by either uniform or Gaussian probability distribution functions (PDFs) within appropriate parameter ranges derived from MeBo drilling and core sample analysis. This accounts for the fact that the input parameters have uncertainties and that the same set of Archie's coefficients might not apply to the larger sediment volume measured by the CSEM remote sensing technique compared to drilling.

Similar to Sava and Hardage (2007), we use uniform distributions for the resistivity of the pore fluid ρ_ω, the resistivity of clay R_c and Archie coefficients *a*, *m*, and *n*. The formation factor – porosity - relationship of the MeBo core data shows that *a* and *m* are interdependent. We therefore sample from a range of *a* – *m* combinations that envelope the range of the MeBo-17/19 core data (see Supplementary Materials). Gaussian distributions are applied to the logarithm of the formation resistivity log10 ρ_f, the porosity ϕ, and the volume of clay V_c. Saturations are then estimated running Monte Carlo simulations over the PDFs by repeated (N=5000) calculations of Archie's relationship using both the clean sand formulation in eq. 3 and shaly sand correction in eq. 5. The resulting saturations are binned in 1% intervals. Negative saturations

which may result mathematically are excluded from binning, and the probability density distribution and 68% confidence intervals are then calculated from the positive bins.

4. 2D CSEM Inversion

We use the open-source 2D inversion code MARE2DEM (Key, 2016) to calculate the electrical resistivity models from the CSEM data. The code makes use of an Occam-type regularization (Constable et al., 1987) to derive smooth models of minimum spatial contrasts which fit the data within the given error structure. This is accomplished in two phases. In the first phase the target misfit is reached by a stepwise line search of the Lagrange parameter by minimising both the root-mean- square (*rms*) misfit and the model roughness. In the second phase, the algorithm seeks a model at the target misfit with the smallest roughness norm (Key, 2016). Model discretization is done optionally by unstructured triangular or quadrilateral grids, or both, which allows more flexibility to adapt to seafloor topography and complex model structure, while minimizing the number of grid cells.

Control of the inversion process can be attained in different ways: i) Convergence of the inversion process can be facilitated by increasing the target misfit or assigning a relative error to the statistically derived absolute data error (e.g. Connell and Key, 2013). This accounts for systematic errors including geometry, navigation and time delays which are not encountered by the standard deviations derived from stacking alone. ii) Changing the spatial smoothness constraint is particularly effective, if the model cells have large horizontal to vertical ratios. iii) The code allows to invert for isotropic, bi-, and triaxially anisotropic models using a penalty weight factor that controls the size of the anisotropy ratio. iv) A-priori known model parameters can be fixed or confined within a given parameter range, and v) weighted penalty cuts can be applied across model segments from e.g. reflection seismic boundaries (see Key, 2016, for details).

4.1 Inversion input parameter

The following parameters were used as input in the inversion:

Journal Pre-proof

- For all inversion results shown in the following paragraph the starting model contained an air layer with a fixed resistivity of 10^5 Ωm.
- Seawater resistivities of 0.4 Ωm were measured at the seafloor with the CTD –sensor inside the pig and showed little variation along the profiles. Thus, the value was fixed for the ocean layer in the starting models which is feasible as both transmitter and receivers are towed on the seafloor. However, we also tested a layered ocean model which didn't change the inversion results.
- We use the MeBo-19 resistivity log to derive a starting model for in the shown inversion results. It contained seafloor parallel layers of increasing resistivity from 1 to 15 Ωm within the upper 50 mbsf, 17 Ωm down to ~500 mbsf and 5 Ωm outside the resolved areas (Table 2). We initially tested a homogeneous half-space of 3 Ωm as starting model, but data fit and convergence improve with the starting model adapted from the MeBo-19 resistivity log.
- A combination of triangular, quadrilateral and again triangular elements are used to finely discretize the shallow layers, the deeper area covered by the data, and model areas outside the range covered by the data, respectively. This accounts for data sensitivity to resistivity changes close to the seafloor, model resolution, and size of the inverse problem. Bathymetry and array geometry including dip angles of the dipoles are this way considered in the starting model.
- We invert eight logarithmically spaced frequencies from 0.167 to 300 Hz for profile P1, and 0.167 to 55.5 Hz for profiles P2 and P3, but omit the highest frequencies for receiver R4 at profiles P1 and P2.
- The horizontal to vertical penalty weight was varied between 1 and 10. The higher the penalty weight the smoother is the lateral contrast in the model. The average aspect ratio of the vertical to horizontal length of the quadrilateral grid cells is 1:5 in all models, therefore a penalty weight of 5 was chosen in for the inversion of profiles P1, P2, and P3.
- We tested vertical anisotropic inversion using anisotropy penalty weights between 0.1 and 10 (Key, 2016). For all three profiles we found isotropic inversion results that could fit the data to the same

331 degree as the vertical anisotropic inversion, thus isotropic inversion is applied in the inversion
332 results shown in Figures 3, 4, and 5.

333

334 *Table 2: Parameters of the layered starting model used in the inversions. Resistivities and ranges are taken*
335 *from the MeBo-19 resistivity log and range of background models.*

Layer	Depth range	Resistivity Start model	Allowed resistivity range
Air	-	100000 Ωm	fixed
Ocean	-	0.4 Ωm	fixed
1	0 – 5 mbsf	1 Ωm	0.3 – 2 Ωm
2	5 – 15 mbsf	3 Ωm	0.5 – 10 Ωm
3	15 – 30 mbsf	8 Ωm	2 – 20 Ωm
4	30 – 50 mbsf	15 Ωm	5 – 30 Ωm
5	>50 mbsf	17 Ωm	5 - 50 Ωm
6	Outside model range	5 Ωm	1 - 100 Ωm

336

337

338 *4.2 Sensitivity Matrix*

339 The sensitivity matrix or Jacobian provides a measure which parts of the model are sensitive to the data.
340 The matrix contains the derivatives of all data with respect to all model parameters

341 $$\left(S_{i,j} = \left\{\frac{\partial f_i}{\partial \log 10\, m_j}\right\}, i = 1.... N; j = 1.... M\right), \quad (6)$$

342 where N is the number of data, and M is the number of model parameters. Logarithms of both data and
343 model parameters are used according to their logarithmic distribution. Cumulative sensitivities are
344 calculated by summing up each column of the sensitivity matrix (containing data for different components
345 and frequencies) and scaled with the data errors and the area of the respective grid cell. This provides a
346 measure of the average sensitivity of all data with respect to each model parameter for the respective model
347 under consideration, and can be used to exclude model parts with low sensitivity from interpretation

Journal Pre-proof

(Schwalenberg et al., 2002). However, the threshold up to which sensitivity value the model is resolved by the data is not clearly defined and subject to the users experience. We used a threshold of 10^{-3} of the normalized cumulative sensitivity to exclude model parts with smaller sensitivity from the interpretation.

5. Results

5.1 Working Area 1 – S1 Channel

Journal Pre-proof

356

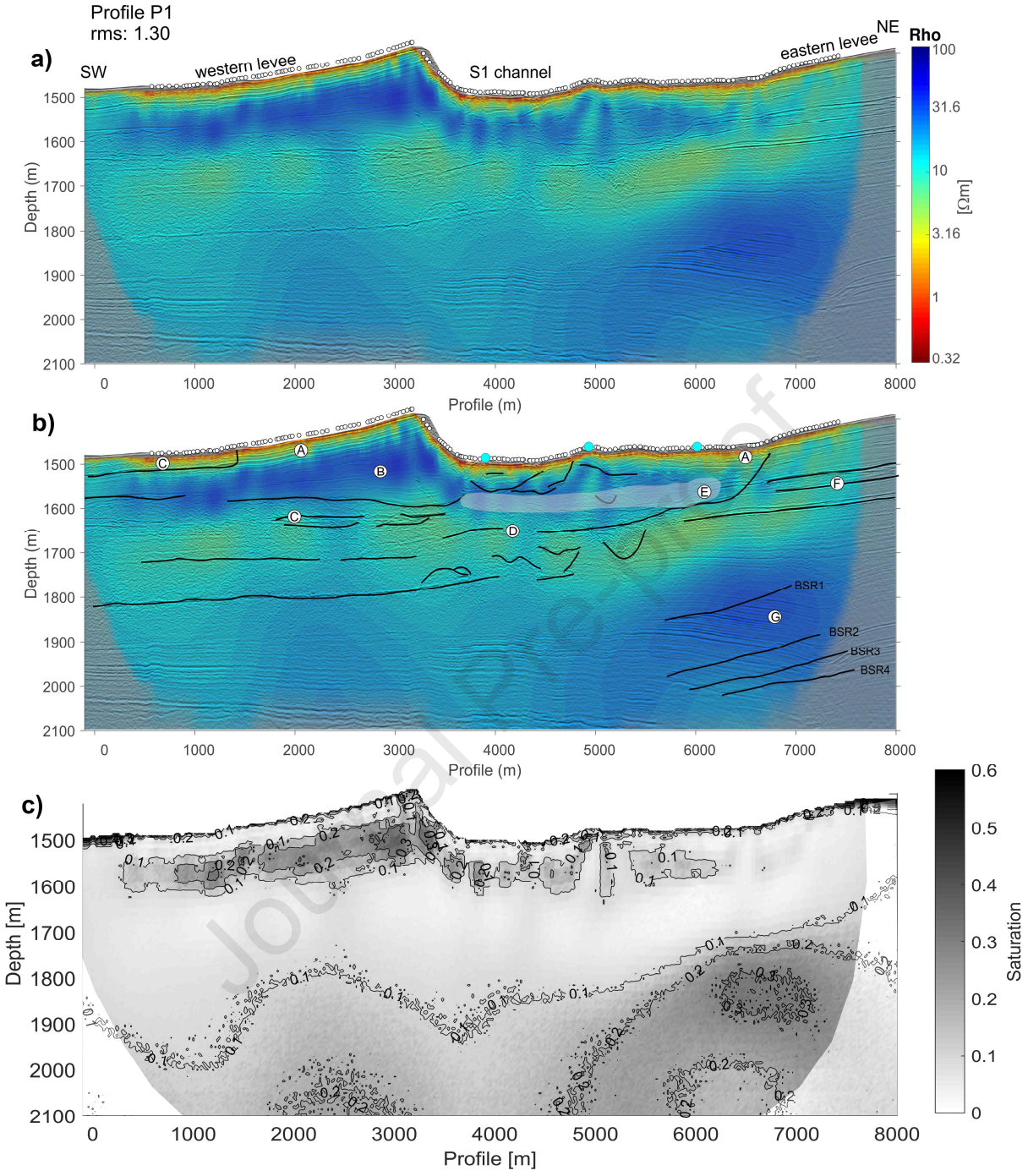

357

358 *Figure 3: a) Resistivity model from 2D inversion of profile P1 across the S1 channel (see Figure 1 for*
359 *location) overlaid with coincident MCS line 1107 (Zander et al., 2018, this issue). Open circles at the*
360 *seafloor mark transmitter positions. b) Interpretation of Figure 3a: (A) transition of conductive to more*
361 *resistive sediments (~1-10 Ωm) within the upper ~40 mbsf are caused by the decrease in salinity from 22 to*
362 *~2.5 psu. (B) a zone of fine grained homogeneously layered levee sediments below the western levee*
363 *corresponds with high resistivity values (20-30 Ωm) at depths from ~1500-1600 m (~50-150 mbsf). (C)*

MTDs of irregular seismic facies and low to high amplitudes close to the seafloor and intercalated within deeper levee sediments are conform with resistivity values in the range of 10-20 Ωm. (D) Sediments below the S1 channel are characterized by meandering sub channels caused by abundant levee failures and channel cuts. CSEM inversion reveals a layer of high resistivities (~18-25 Ωm) from 1550 – 1650m (~50-150 mbsf) which terminates towards the eastern levee. The lateral extension of the layer is in good agreement with a P-wave velocity anomaly (E) derived from OBS data (light blue dots, Bialas et al., 2020, this issue*). Below the eastern levee resistivities are lower (~10 Ωm) where older levees are imaged by strongly stratified sediments (F). At depths below ~1750 m resistivities increase again towards the stack of multiple BSRs (G). c) Saturation model derived with the stochastic approach of Archie's relationship using the clean sand formulation. Saturation estimates are in the order of 10-20% within the sediments below the western levee increasing towards 30% below the ridge, 10% at depths from 50-150 m below the S1 channel, and locally 20-30% below the eastern levee starting ~100 m above the recent BSR 1. Transparency has been added to model parts with a cumulative sensitivity less than 10^{-3}.*

Profile P1

Figures 3a and 3b show the 2D inversion result of profile P1 in WA1. Profile P1 covers the S1 channel and parts of the outer levees. The profile coincides with the 2D multi-channel seismic (MCS) line 1107 (Bialas, et al., 2014; Zander et al., 2017; Figure 1) which is overlaid on the resistivity model (see Table 1 for inversion details).

Hillman et al. (2018, this issue) classified the key sedimentary facies in the Danube fan as follows: i) Mass transport deposits (MTDs) are slope failure events which are characterized by chaotic and irregular seismic facies with discontinuous low to high amplitude reflections; ii) Channel fill sediments (CFS) are associated with turbidity current deposits within the canyons characterized by sub-parallel, irregular reflections along narrow belts with high seismic amplitudes. Sediments are predominantly coarse-grained clastics with high proportions of sand; iii) Levee deposits (LD) are predominantly finely-laminated, fine-grained spill-over

turbidites which may occasionally contain thin, sand-rich intervals that can act as permeable pathways and seismic data show parallel to convergent, laterally continuous reflections of low to medium amplitudes.

The resistivity model of profile P1 (Figures 3a and b) shows conductive sediments in the upper 30 mbsf with resistivities of 1-3 Ωm. This shallow part is characterized by stratified fine-grained levee sediments with thin intercalated clay-dominated layers and MTDs. At depths below ~50 mbsf the CSEM model shows an abrupt transition to an about 100-150 m thick layer of higher resistivities around 20-30 Ωm. Below the western levee this layer is seismically characterized by predominantly laminated levee sediments, while the area below the S1 channel is dominated by sequences of meandering channel fills and faulting from heavy sedimentation rates. Below the eastern levee resistivity values are lower at the same depth where seismic layering becomes horizontally stratified. At depths below ~150 mbsf (1600-1650 m depth) higher conductivities below the western levee occur where the seismic section shows alternating levee deposits and MTDs. The transition to elevated resistivities below the western levee is in fairly good agreement with a seismic discontinuity at depths of 1820 m. Below the S1 channel inversion revealed elevated conductivities within a broader zone of paleo channels below ~ 200 mbsf (~1650 m depth). Resistivities increase again below the discontinuity. At depth below the eastern end of the profile resistivities increase to values around 20 Ωm where reflection seismic data display a stack of multiple BSRs.

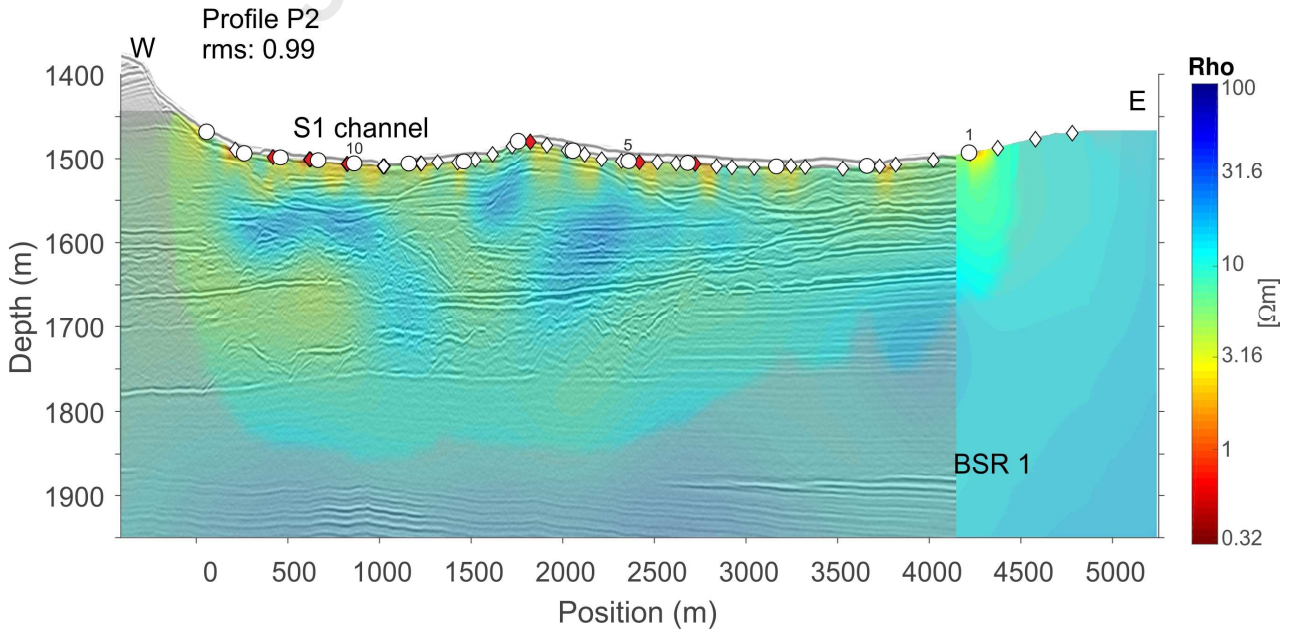

Journal Pre-proof

Figure 4: 2D inversion result of profile P2 across the S1 channel (see Figure 1 for location) using stationary data of receivers R1, R3, and R4 (see Table 1). The coincident 2D seismic line cut out from the 3D seismic cube has been overlaid (Bialas et al., 2014). Transparency has been added to model parts with a cumulative sensitivity less than 10^{-3}. White circles mark transmitter positions and triangles mark receiver positions. Missing receiver data of R3 are marked in red.

Profile P2

Profile P2 runs in E-W direction across the S1 channel and intersects with profile P1 at the footstep of the ridge (Figure 1b). Data sensitivity and model resolution is lower compared to profile P1 due to data gaps of receiver R3 caused by an instable connection to one receiver electrode. Also, no roll-on data could be used in the inversion (see Table 1 for inversion details).

The resistivity model in Figure 4 confirms the general trend observed on profile P1 in Figure 3 of lower resistivities (1-3 Ωm) within the upper 30 mbsf and a layer with higher resistivities at depths from ~1550 m to 1680 m (~50-150 mbsf) which is laterally interrupted due to low model resolution rather than to real structure. The overlaid seismic section is taken from the 3D cube (Bialas et al., 2014) and shows a similar stratigraphy compared to the 2D MCS section overlaid in Figures 3a and b. However, we don't see a clear correlation between the resistivity patterns and seismic features and do not further refer to this model in the discussion, but decided to present it for completeness.

5.2 Working Area 2 – S2 Slump Area

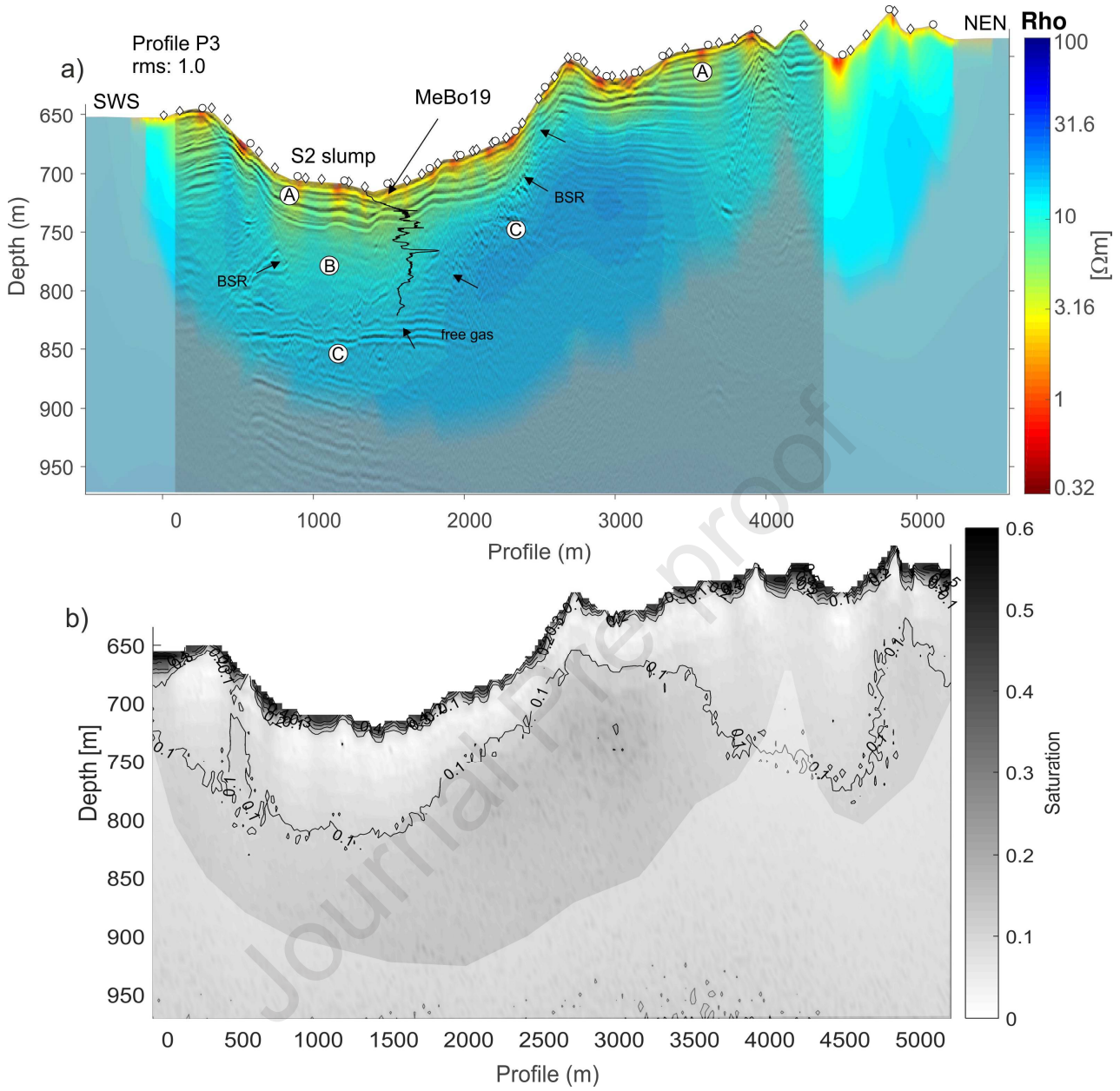

Figure 5: a) 2D inversion result and interpretation of profile P3 across the S2 slump overlaid with the coincident seismic line taken from the 3D cube (Bialas et al., 2014). Open circles and diamonds at the seafloor mark transmitter and receiver positions, respectively. The MeBo-19 resistivity log (Bohrmann et al., 2018) has been projected on the figure (see Figure 1 for location). (A) Transition of conductive to more resistive sediments (~1.5-8 Ωm) within the upper ~40 mbsf are caused by the decrease in salinity from 22 to ~2.5 psu which agrees with the MeBo 19 resistivity log, and corresponds with stratified levee sediments with higher clay content (Riedel et al., 2020, this issue*). (B) Within the S2 slump, resistivities are fairly*

homogeneous around 10-14 Ωm and correspond with seismically homogeneous levee sediments. (C) Resistivities increase to values of 15 Ωm below the depth of the BSR which steeply bends towards the seafloor where it outcrops at profile meter 2500. b) Saturation estimates derived with the stochastic approach of Archie's relationship. Gas hydrate saturations are around 0% within the GHSZ. Below the BSR saturations increase slightly to values of less than 10% which could indicate low gas concentrations. Transparency has been added to model parts with a cumulative sensitivity less than 10^{-3}.

Profile P3

Figure 5a shows the inversion results of profile P3 in WA2. The profile is located in water depths from 580-700 m and covers the S2 slump area and the landward edge of the gas hydrate stability field. Data at 19 waypoints from only two receivers R1 and R2 are available. The corresponding seismic section cut out from the 3D cube has been overlaid on the resistivity model.

Similar to the profiles in WA1 we observe a good correlation between conductive sediments with values increasing from 1.5-3 Ωm to 6-9 Ωm and younger stratified levee deposits within the upper 40 mbsf. The transition of conductive to resistive sediments appears at the same depth range in the MeBo-19 resistivity log drilled about 1 km to the east (see Figure 1c) which has been projected on the model. Below the S2 slump area, resistivities generally increase from 10 to 14 Ωm at depths from 40 mbsf to the BSR. This corresponds with homogeneous levee sediments in the seismic section. Patches of high amplitude reflections at depths of ~820 m and at the flanks of the slump area mark the BSR which steeply bends towards the seafloor where it outcrops at profile meter 2500. Resistivities remain constant at 15 Ωm below the depths of the BSR which was found at 144 mbsf at site MeBo-17 (Bohrmann et al., 2018), but the resistivity model has low resolution at greater depths as low sensitivities show.

5.3 Background Resistivity Models from MeBo drilling

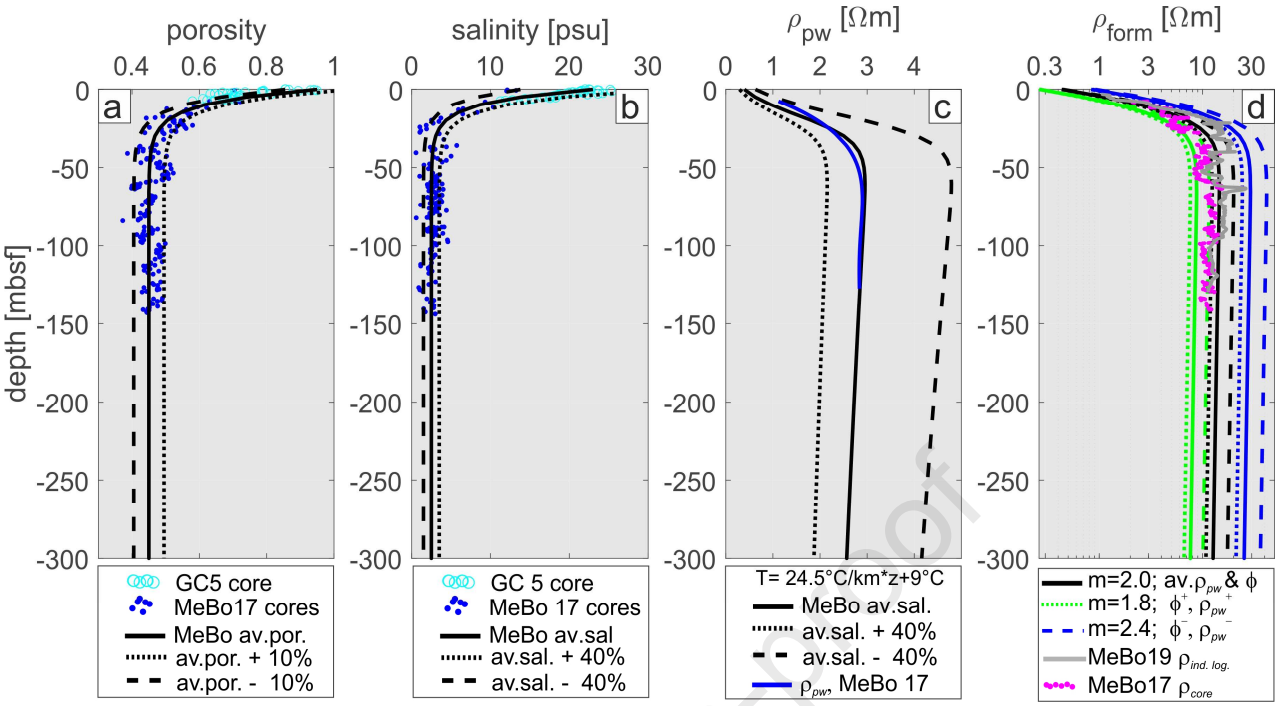

Figure 6: a) Porosity data derived from gravity core GC5 and MeBo-17 cores in WA2, average porosity (av.por.) and variations of +/-10% of the average. b) Salinity data derived from GC5 and MeBo-17, average salinity (av.sal.) and variations of +/-40% of the average. Below ~40 mbsf salinity values are in the range of 1.5-3.5 psu and 2.5 psu on average. c) Pore water resistivity–depth profiles derived with Gibbs seawater toolbox (McDougall and Barker, 2011) using the average salinity and variations in b) and the thermal gradient given in Zander et al. (2017). d) Background resistivity-depth profiles calculated with Archie's relationship using average porosities in a) and pore water resistivities in c) (solid lines), upward variations (dotted lines) and downward variations (dashed lines). Green, black and blue refer to cementation factors m= [1.8, 2.0, 2.4], respectively. The gray line shows the deep penetration induction log of MeBo-19, purple dots display the corrected resistivities derived from core samples at site MeBo-17. Core data of GC5 and MeBo-17/19, and the resistivity log of MeBo-19 were supplied by M. Haeckel and M. Riedel (pers. comm.).

We use core data from MeBo-17 and gravity core GC5 located at the western flank of the S2 channel in 765 m water depth (see Figure 1c) to derive a range of background resistivity models. Figure 6a shows core derived porosity data which on average decrease from ~75% at the seafloor to 45% at ~40 mbsf and stay

nearly constant below. The variability is about +/-10%. Salinities shown in Figure 6b decrease from 22 psu at the seafloor which agrees with Popescu et al. (2006) and Soulet et al. (2010) to nearly freshwater values of 2.5 psu on average below ~40 mbsf. Here, the salinities vary between 1.5 and 3.5 psu or +/- 40% from the average which is within the range derived from piston cores at the landward edge of the GHSZ (1-4 psu, Ker et al., 2019).

Pore water resistivities (Figure 6c) were calculated with the Gibbs seawater oceanographic toolbox (McDougall and Barker, 2011) using the average salinity values from the cores and variabilities given above, a seafloor temperature of T = 9° C and a geothermal gradient of ΔT=24.5° C/km (Zander et al., 2017). The calculated pore water resistivity at the seafloor is 0.4 Ωm which is in full agreement with the resistivity measurements of the CTD-probe attached to our CSEM seafloor array. Pore water resistivities increase below ~40 mbsf to values of 2.9 Ωm (2.1 and 4.7 Ωm, respectively, for salinity variations of ± 40%).

Archie's relationship in eq. (1) has been used to derive a range of background resistivity-depth profiles (Figure 6d). Input parameters are the average porosity profile and variations (Figure 6a), and the average pore water resistivity profile and variations (Figure 6c). We set Archie coefficients a = 1.0 and m = [1.8, 2.0, 2.4] in addition to the minimum and maximum estimates of pore water resistivities and porosities to obtain a range of realistic background models. This is in agreement with Archie coefficients Riedel et al. (2020, this issue) derived from MeBo-17 core samples (a = 1.045 and m=1.875). The resistivity profiles measured with the deep penetration induction log (Bohrmann et al., 2018) at site MeBo-19 and the corrected core-derived resistivities of Site MeBo-17 are within the range of the calculated background resistivity models, but do not follow one particular background model (using single porosity and salinity trends and a constant cementation factor). Particularly within the first 40 mbsf, log and core derived resistivities cover a range of background models. Deeper than 50 mbsf the resistivity log is closest to the background resistivity derived with the average porosity and salinity and m = 2.0. Varying the cementation factor m seems to have a smaller effect on the formation resistivity than variations of porosity and salinity (comparing line styles of same colors in Figure 6d).

In the following we investigate, if the inverted resistivity models of profiles P1 and P3 can be explained by the range of background models in Figure 6d or possibly indicate the presence of gas hydrate and free gas.

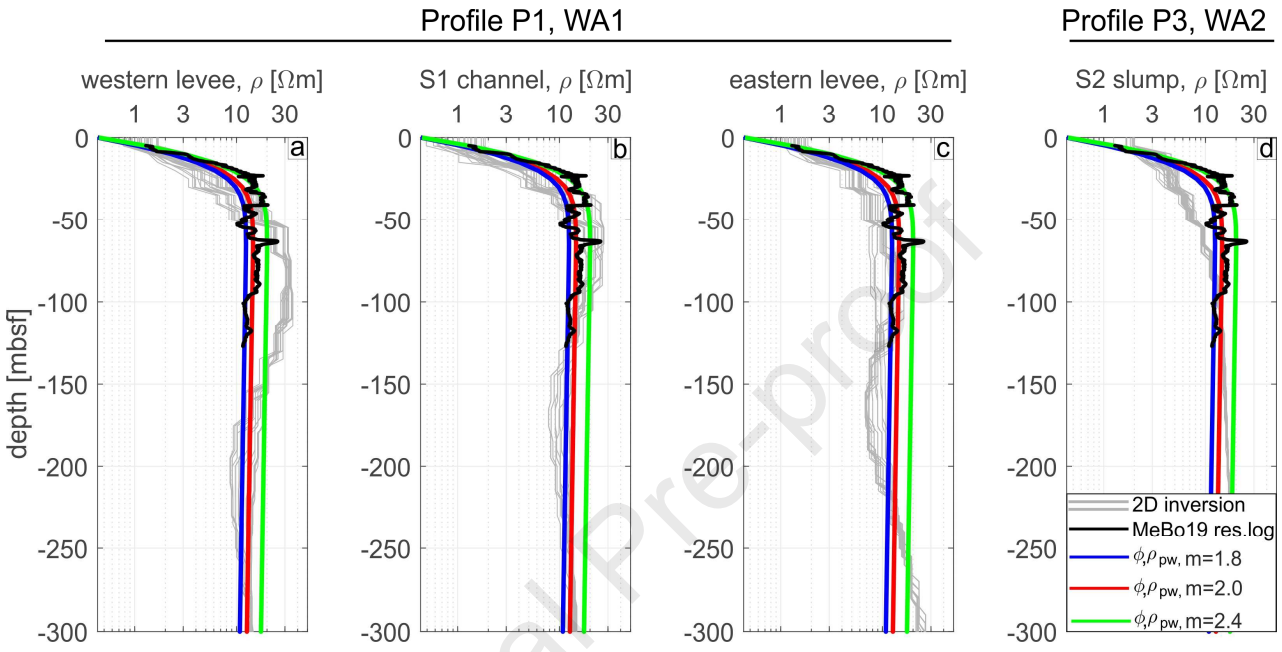

Figure 7: Background resistivity depth profiles calculated with the average porosity and pore water resistivity profiles in Figure 6 and cementation factors m = [1.8, 2.0, 2.4] (colored lines) and the MeBo-19 deep penetration resistivity log (black) compared with selected subsets of the inverted resistivity models of profiles P1 and P3 (gray lines). a) P1 western levee, profile meter 2000-2500; b) P1 S1 channel, profile meter 4000–4500; c) P1 eastern levee, profile meter 6700–7200; d) P3 S2 slump, profile meter 1200–1700.

5.4 Comparing Inverted Resistivity and Background Models

In Figure 7 we compare the background models derived from the average porosity and pore water resistivity models and different cementation factors (Figure 6d) with selected subsets of the inverted resistivity models of profiles P1 (Figures 7 a-c) and P3 (Figure 7d). We thereby assume that the general porosity and salinity distributions are not too different between the two working areas. This might be justified as reflection seismic profiles from both areas show similar features including pronounced shallow

levee deposits, sequences of mass transport deposits, and older levee deposits (Hillman et al., 2018, this issue).

The inverted resistivities are generally lower than the background models within the upper 40 mbsf where salinities and porosities change rapidly. We attribute this to the roughness constraint in the Occam inversion which impedes strong resistivity contrasts (Constable et al., 1987). At profile P1, inversion revealed higher than background resistivities at depths from ~50 – 150 mbsf below the western levee (Figure 7a) and ~50 – 100 mbsf below the S1 channel (Figure 7b). Below the eastern levee, resistivity values remain below the background and increase at depth > ~250 mbsf (Figure 7c). At profile P3, below the S2 slump, the inverted resistivities are in the range of 5-10 Ωm and still lower than the MeBo-19 resistivity log and the background resistivities from ~25-100 mbsf. Below 100 mbsf, the inverted resistivities are constant, but lose sensitivity with depth. (Figure 7d).

5.5 Gas Hydrate Saturation Estimates

In order to predict if and how much gas hydrate or free gas is present in WA1 and WA2 we derive saturation estimates from the resistivity models of profiles P1 and P3 applying the stochastic approach after Sava and Hardage (2007) presented in section 3.6 using the following parameter ranges as input in Archie's relationship:

Table 3: Parameter input ranges used in the stochastic calculation of saturation estimates

Porosity Φ	Pore water resistivity ρ_w	Archie coefficients *a/m*	Saturation factor *n*	Volume fraction clay V_c	Resistivity clay R_c	Formation resistivity ρ_f Subsets	Formation resistivity ρ_f Models
MeBo average +/- 10%	MeBo average +/- 40%	[0.8 / 2.5] to [1.2 / 1.5]	2.0-2.5	0.1–0.6	5-60 Ωm	[min log ρ_f - max log ρ_f]	log ρ_f +/- 10%
Gaussian	Uniform	Uniform	Uniform	Gaussian	Uniform	Gaussian	Gaussian

- The porosity Φ follows the average MeBo-derived porosity-depth function (Figure 6a) and is assigned to a Gaussian distribution in the range of the average porosity +/- 10%.
- The pore water resistivity depth function ρ_w has been converted from mean salinity values at site MeBo-17 (Figure 6c) and is assigned to a uniform distribution in the range of the average pore water resistivity +/- 40%.
- The formation factor - porosity relationship derived from core data of site MeBo-17/19 suggests that a wider range of *a*-*m* combinations applies to the core samples, and that Archie coefficients *a* and *m* vary not independently from each other (see Supplementary Materials). We use uniformly distributed combinations in the range of [a = 0.8, m = 2.5] and [a = 1.2, m = 1.5].
- According to Cook and Waite (2019) we assume a uniform distribution for the saturation exponent in the range of n = [2.0 2.5].
- The formation resistivity ρ_f is assigned to a Gaussian distribution in the log10 range. In Figure 8 resistivity ranges are taken from the subsets shown as gray line in Figure 7. For the saturation models shown in Figures 3c and 5b we assign a range of log10 ρ_f +/- 10% to the inverted resistivities of the corresponding models in Figure 3a and 5a.
- For the shaly sand correction we apply a Gaussian distribution in the range of V_c=[0.1 0.6] for the volume fraction of clay (Ker et al., 2019) and a uniform distribution in the range of R_c=[5 60] Ωm for the resistivity of clay.

Journal Pre-proof

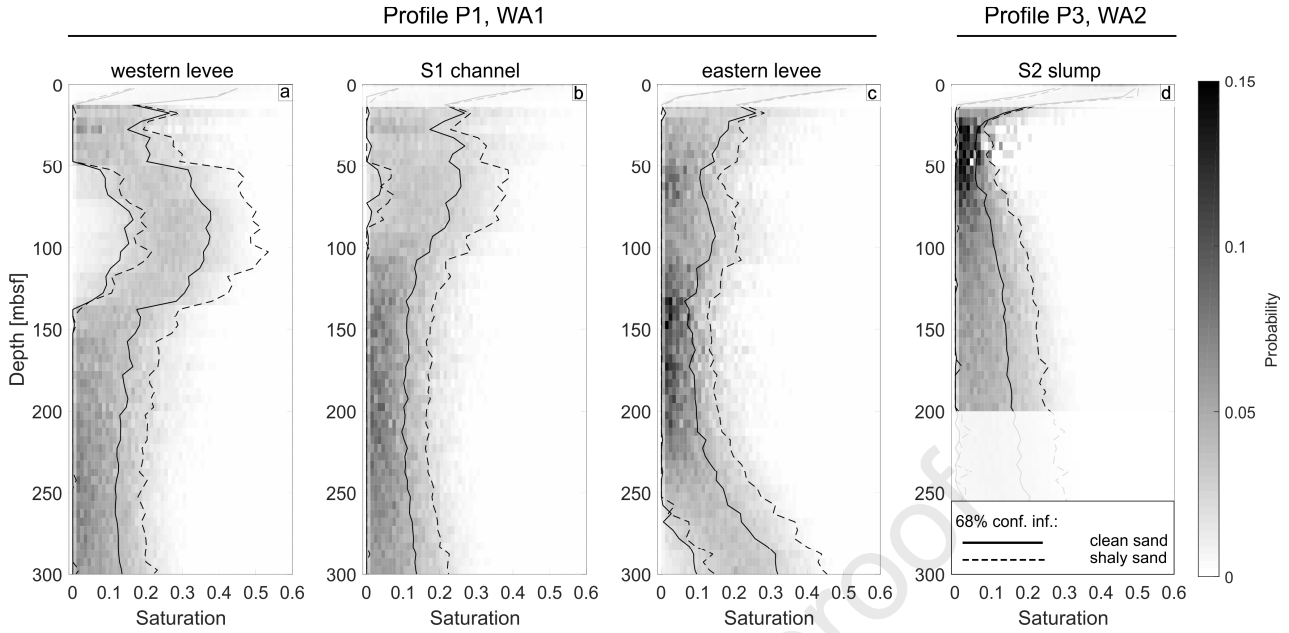

Figure 8: Probability density distributions following Sava and Hardage (2007) of saturation estimates derived from subsets of the resistivity models of profile P1 a) western levee, b) S1 channel, c) eastern levee, and profile P3 d) S2 slump . Solid and dashed lines mark the 68% confidence intervals calculated with the clean sand and shaly sand correction using eqs. (3) and (5), respectively. High saturations within the upper ~20 mbsf result from the roughness penalty impeding strong resistivity contrasts in the inversion (see text for details).

Saturation estimates have been calculated using Archie's relationship from 5000 random samples of the parameter ranges given above and in Table 3. The resulting saturations have been grouped in 1% intervals from 0 to 100%. Negative saturations can result mathematically, but are unrealistic and have been excluded from binning. A probability density function and 68% confidence intervals have been calculated for each model parameter.

We present the saturation estimates for profiles P1 and P3 in profile view in Figures 3c and 5b, and as saturation depth profiles in Figure 8. The saturation models for profile P1 in Figure 3c and for profile P3 in Figure 5b show the median of the confidence interval derived with the clean sand formulation in eq. 3. Probability density distributions and confidence intervals in Figure 8 have been derived from the same data subsets of profiles P1 and P3 used in Figure 7. The confidence intervals show that the saturation estimates

have uncertainties of 15 - 20% given the range of input parameters. Depth ranges with higher probabilities go along with smaller uncertainties. Comparing the confidence intervals derived with the clean sand formulation (eq. 3, solid black line) with the shaly sand correction (eq. 5, dashed black lines) yields about 10% higher saturation estimates including clay in the calculation. High saturation estimates close to the seafloor result from the roughness penalty constraint in the Occam inversion suppressing strong resistivity contrasts in the models and are excluded from our interpretation.

Saturation Estimates, Profile P1

The saturation model for profile P1 in Figure 3c shows saturations of 10-20% within the resistive layer below the western levee. Below the ridge saturations rise locally up to 30%. The ridge topography and the seafloor array geometry are included in the model, but may contribute to the high resistivity and saturation values below the ridge. Below the S1 channel, saturations are around 10% at ~1550 m (50-150 mbsf) within a layer that terminates towards the eastern levee. Another zone of higher saturations of up to 30% has been revealed below the eastern levee at depths of the recent BSR (1800 m). The probability distribution with depth and confidence intervals of the model subsets in Figure 8 a-c reflect the saturation model in Figure 3c, but also illustrate the uncertainty width of the saturation estimates given the input parameter ranges.

Saturation Estimates, Profile P3

The saturation model for profile P3 in Figure 5b shows low to negligible saturations below 10% within the GHSZ and towards the northeast of the profile outside the gas hydrate stability field. Only at depths below the BSR saturations are in the order of 10% and higher, but sensitivity of CSEM data decays below ~850 m (~200 mbsf). The probability density distribution in Figure 8d indicates a general increase in saturation below ~30 mbsf and fairly wide confidence intervals.

6. Discussion

Inversion of geophysical data is inherently non-unique. Thus we should state that the resistivity models derived from 2D inversion in Figures 3, 4, and 5 are also non-unique, but reflect the smoothest possible

resistivity distribution at the target misfit (Constable, 1987), and impedes strong resistivity contrasts. Model resolution also decays with depth as reflected by the sensitivity matrix which is used to mask model parts of low sensitivity to the data. Including roll-on data in the inversion of profile P1 improved model resolution and data sensitivity to greater depth. Inversion of "only" stationary data and missing data at greater transmitter receiver offsets at profiles P2 and P3 reduced model resolution and sensitivity at depth.

Saturation estimates based on Archie's relationship depend on the knowledge of the input parameters or a valid background resistivity model. Background models derived from porosity and salinity data of site MeBo-17/19 in WA2 show large variabilities, also for different cementation factors. Comparing the MeBo-19 resistivity log with the background models demonstrates that a single set of input parameter in Archie's relationship may not apply to calculate saturation estimates from our resistivity models covering different lithologies (Figure 6d). We therefore adopt the stochastic approach of Sava and Hardage (2007). Uncertainties of the input parameter in Archie's relationship are expressed by either uniform or Gaussian probability distribution functions, and saturation estimates are derived from the confidence intervals of the randomly determined probability distributions.

The resistivity model of profile P1 in WA1 generally reflects the transition of marine to lacustrine pore waters within the top 30-40 mbsf (salinity drops from 22 psu to 1.5-3.5 psu) and the decrease in porosity from ~70% to 45%. MSC data show strong reflections and smaller intercalated mass transport deposits. Sediments are likely clay-dominated assuming a similar stratigraphy as in WA2, but drilling data are missing in WA1. The presence of gas hydrates can be discarded in this shallow section.

Below the western levee and S1 channel, 2D inversion revealed anomalously high resistivities within a ~100 m thick layer at about 50 mbsf which fades out towards the eastern levee (Figure 3a). We derive saturation estimates around 20% below the western levee, 30% below the ridge, and around 10% below the S1 channel with 15-20% wide confidence intervals around the median (Figure 8). Including clay in the calculation shifts the estimates by ~10% towards higher saturations. Below the western levee, the well-resolved resistive layer is conform with a zone of homogeneously layered, fine grained levee sediments intercalated with smaller mass transport deposit. Gas hydrates saturations in the order of 20-30% seem unlikely within the fine grained sediments with probably high clay content. Reduced permeabilities and

porosities in the order of 30-35% caused by higher compaction due to different sedimentation rates at the western levee may also explain the resistive layer, but seismic velocity information and drilling data are missing which would help to clarify the origin of the high resistivities, and whether they are caused by gas hydrate, low porosity, or possibly a mixture of both.

Below the S1 channel, the resistive layer shows high spatial agreement with the extent of an anomalous P-wave velocity layer (Figure 3b, Bialas et al., 2020, this issue). The resistive layer terminates where reflection seismic data show a lateral transition from multiple levee failures and channel cuts to rather stratified levee sediments east of profile meter 6200 in Figure 3. Dannowski et al. (2017) derived 6-12% pore filling gas hydrates for the high velocity layer which is in good agreement with the saturation estimates around 10% derived from the CSEM data at profile P1, but lower than Duan et al. (this issue) derived from an independently analyzed 3D CSEM data set.

Another zone of higher resistivities occurs at greater depth below the eastern levee where a stack of multiple BSRs is visible in the seismic section. Saturations are 10-20% reaching a local maximum of 30% at the recent BSR-1 which we explain with gas hydrates above and free gas below the BSR. Interestingly, elevated resistivities are centered around the area where the multiple BSRs are clearly visible in the seismic section which may imply locally higher gas hydrate and free gas concentrations in connections with the observable BSRs.

The resistivity model of profile P3 in WA2 shows a generally smooth increase in resistivity with depth at the S2 slump compared to the sharp increase observed in the background resistivity models and resistivity log at site MeBo-19 (Figure 6d). The smooth trend is attributed to the smoothness constraint in the inversion and availability of data from only two receivers. The increase in resistivity with depth is mainly controlled by the decrease in salinity and porosity (Figures 6 a, b). Saturation estimates revealed little to no (<10%) gas hydrate within the GHSZ at the bowl-shaped S2 slump. MeBo drilling at site 17/19 also did not provide clear evidence of gas hydrates (Riedel et al., 2020, this issue). The reflection seismic section extracted from the 3D cube shows strongly stratified levee sediments within the upper 30-40 mbsf (Figure 5a). Drilling at site MeBo-17/19 revealed clay-dominated sediments in the shallow part (Riedel et al. 2020, this issue). At depths from ~40 mbsf to the BSR at 144 mbsf seismic data show a well stratified unit of fine-

Journal Pre-proof

grained sediments of channel-overspill turbidites with an underlying MTD of lower reflection amplitude (Riedel et al., 2020, this issue). Interestingly, the bowl-shaped upward bending BSR seems to mark a boundary to generally higher resistivities in the inversion model which goes along with slightly higher saturation estimates above 10%. Together with the enhanced amplitude reflections and polarity changes observed in the seismic section this possibly indicates that some amount of free gas has accumulated below the base of the GHSZ.

7. Summary and Conclusions

We analyzed marine time domain CSEM data of three profiles in two working areas from the offshore Danube fan using state of the art 2D regularized inversion (MARE2DEM, Key, 2016) with the aim to identify possible gas hydrate occurrences and to provide saturation estimates. The resulting resistivity models were compared with coincident reflection seismic sections (Bialas et al., 2014, Zander et al., 2017), and drilling data from site MeBo-17/19 in WA2 offshore Romania (Bohrmann et al., 2018, Riedel et al., 2020, this issue). To derive saturation estimates we applied a stochastic approach of Archie's relationship (Archie, 1942) after Sava and Hardage (2007) which considers uncertainties in the input parameters. Our most significant findings are:

- The resistivity values are generally higher compared to other gas hydrate regions as a consequence of low pore water salinities introduced by sea level low stands during the last glacial maximum.
- The transition of lower to higher resistivities from seafloor to 30-40 mbsf of the inverted resistivity models reflects the sharp decrease in porosity and salinity as observed in MeBo drilling data in WA2.
- Below the S1 channel in WA1 a resistive layer at intermediate depths indicates gas hydrate saturations in the order of 10% within a sediment section dominated by meandering channel fills and faulting. This is in agreement with saturation estimates derived from a seismic P-wave anomaly (Bialas et al., 2020, this issue), and somewhat lower than saturation estimates derived from an independent 3D CSEM data set (Duan et al., this issue).

- The resistive layer extends below the channel ridge and western levee where saturation estimates are 20% and higher. The overlapping seismic section shows a layer of fine grained levee sediments with intercalated smaller mass transport deposits. Whether gas hydrates or a denser lithological unit of decreased porosity caused the anomalous resistivities requires further input from e.g. seismic velocity data and/or drilling.
- Another area of higher resistivities occurs below the eastern levee and coincides with a stack of multiple BSRs and suggests the presence of gas hydrate above and free gas below the recent BSR-1.
- Saturation estimates derived from the resistivity model across the S2 slump area in WA2 reveal no notable saturation values within the GHSZ which is in agreement with coring data at nearby MeBo sites 17 and 19 where no gas hydrates were evident. Saturation estimates are slightly increased (<10%) below the BSR which steeply bends towards the seafloor indicating the presence of small amounts of free gas.

Acknowledgements

This work was carried out in the framework of the SUGAR project which was jointly funded by the German Federal Ministry of Education and Research (BMBF) and the German Federal Ministry of Economic Affairs and Energy (BMWi) (grants 03G0688A, 03SX320Z). We acknowledge the captain and crew of R/V Maria S. MERIAN voyage MSM 35 for their excellent support to collect the CSEM data. The German Science Foundation (DFG) provided the ship time on R/V MARIA S. MERIAN. Gravity core and MeBo drilling data used in this study were kindly provided by Michael Riedel und Matthias Haeckel. We further wish to thank Nigel Edwards for lending us the backup current transmitter for the cruise and Kerry Key for making MARE2DEM available to the community. Paul Wintersteller and Gerhard Bohrmann are thanked for access to the bathymetry data available at doi.org/10.1594/Pangaea.894399 and doi.org/10.1594/Pangaea.895506. Reviews by Ann Cook, Michael Riedel and the Special Issue Guest

Journal Pre-proof

Editor Matthias Haeckel provided helpful comments and detailed discussions which significantly improved the manuscript.

References

Andreassen, K., Hart, P.E., MacKay, M., 1997. Amplitude versus offset modeling of the bottom simulating reflection associated with submarine gas hydrates. Marine Geology, 137(1-2), 25–40.

Archie, G.E., 1942. The Electrical Resistivity Log as an Aid in Determining Some Reservoir Characteristics. Petroleum Transactions of the AIME, 146, 54-62.

Baristeas, N., 2006. Seismische Fazies, Tektonik und Gashydratvorkommen im nordwestlichen Schwarzen Meer. Diplomarbeit, Universität Hamburg, Germany, 106 pages.

Bialas, J., Klaucke, I., Haeckel, M. (ed.), 2014. FS Maria S. Merian Fahrtbericht/CruiseReport MSM 34/1 & 2 SUGAR Site. Berichte aus dem GEOMAR Helmholtz-Zentrum für Ozeanforschung, Kiel, Germany, Nr. 15, 111 pages.

Bialas, J., Bohlen, T., Dannowski, A., Eisenberg-Klein, G., Gassner, L., Gehrmann, R., Heeschen, K., Hölz, S., Jegen, M., Klaucke, I., Krieger, M., Mann, J., Müller, Ch., Prüßmann, J., Schicks, J., Schünemann, E., Schwalenberg, K., Sommer, M., Smilde, P.L., Spangenberg, E., Trappe, H., Zander, T., 2020. Joint interpretation of geophysical field experiments in the Danube deep sea fan, Black Sea. Marine Petroleum and Geology, this issue. Available online: https://doi.org/10.1016/j.marpetgeo.2020.104551.

Bohrmann, G. (ed.), 2018. R/V METEOR Cruise Report M142, Drilling Gas Hydrates in the Danube Deep-Sea Fan, Black Sea, Varna – Varna – Varna, 04 November – 22 November – 09 December 2017. Berichte aus dem MARUM – Zentrum für Marine Umweltwissenschaften, Fachbereich Geowissenschaften, Universität Bremen, Germany, Nr. 320, 121 pages.

Boswell, R., Collett, T.S., 2011. Current perspectives on gas hydrate resources, Energy & Environmental Science, 4(4), 1206–1215.

Collett, T.S., Ladd, J., 2000. Detection of gas hydrate with downhole logs and assessment of has hydrate concentrations (saturations) and gas volumes on the Blake Ridge with electrical resistivity log data. In Paull, C.K., Matsumoto, R., Wallace, P.J., and Dillon, W.P. (Eds.), Proceedings of the Ocean Drilling Program, Scientific Results, Vol. 164, 13 pages.

Journal Pre-proof

738 Connell, D., Key, K., 2013. A numerical comparison of time and frequency□domain marine
739 electromagnetic methods for hydrocarbon exploration in shallow water. Geophysical Prospecting 61,
740 187-199.
741 Constable, S.C., Parker, R.L., Constable, C.G., 1987. Occam's inversion: A practical algorithm for
742 generating smooth models from electromagnetic sounding data. Geophysics 52(3), 289-300.
743 Cook, A.E., Waite, W.F., 2018. Archie's Saturation Exponent for Natural Gas Hydrate in Coarse-Grained
744 Reservoirs. Journal of Geophysical Research Solid Earth 123(3), 2069-2089.
745 Dannowski, A., Bialas, J., Schwalenberg, K., Gehrmann, R., Zander, T., Kläschen, D., 2017. Shear wave
746 modelling of high resolution OBS data with a comparison to CSEM data in a gas hydrate environment in
747 the Danube deep-sea fan, Black Sea. Presented at the 9th International Conference on Gas Hydrates,
748 Denver, US, June 25-30, 2017.
749 Degens, E.T., Ross, D.A., 1974. The Black Sea - Geology, Chemistry, and Biology. AAPG Memoir, Vol.
750 20.
751 Duan, S., Hölz, S., Jegen, M., Schwalenberg, K., Li, Y., 2019. Study on Gas Hydrate Targets in the Danube
752 Delta with the Sputnik Controlled-Source Electromagnetic System. Marine Petroleum and Geology, this
753 issue, under revision.
754 Edwards, R.N., 1997. On the resource evaluation of marine gas hydrate deposits using sea-floor transient
755 electric dipole-dipole method. Geophysics, 62, 1, 63-74.
756 Expedition 311 Scientists, 2006. Sites U1325, U1327, U1328 and U1329. In Proceedings of IODP, Vol.
757 311, edited by M. Riedel et al., pp. 1–136.
758 Gehrmann, R.A.S., Dettmer, J., Schwalenberg, K., Engels, M., Dosso, S.E., Özmaral, A., 2015. Trans-
759 dimensional Bayesian inversion of controlled-source electromagnetic data in the German North Sea.
760 Geophysical Prospecting 63(6), 1314-1333.
761 Gehrmann, R.A.S., Schnabel, C., Engels, M., Schnabel, M., Schwalenberg, K., 2018. Combined
762 interpretation of marine controlled source electromagnetic and reflection seismic data in the German
763 North Sea: a case study. Geophysical Journal International, 216(1), 218-230.

Journal Pre-proof

764 Goswami, B.K., Weitemeyer, K.A., Minshull, T.A., Sinha, M.C., Westbrook, G.K., Chabert, A., Hesntock,
765 T.J., Ker, S., 2015. A joint electromagnetic and seismic study of an active pockmark within the hydrate
766 stability field at the Vestnesa Ridge, West Svalbard margin. Journal of Geophysical Research, Solid
767 Earth, 120, 6797–6822, doi:10.1002/2015JB012344.
768 Greinert, J., Artemov, Y., Egorov, V., De Batist, M., McGinnis, D., 2006. 1300-m-high rising bubbles from
769 mud volcanoes at 2080 m in the Black Sea: hydroacoustic characteristics and temporal variability. Earth
770 and Planetary Science Letters, 244 (1/2), 1-15.
771 Haeckel, M., Bialas, J., Klaucke, I., Wallmann, K., Bohrmann, G., Schwalenberg, K., SUGAR participants,
772 2015. Gas Hydrate Occurrences in the Black Sea – New Observations from the German SU GAR
773 Project. Fire in the Ice Newsletter, 15(2), 6-9.
774 Heeschen, K.U., Haeckel, M., Klaucke, I., Ivanov, M. K., Bohrmann, G., 2011. Quantifying in-situ gas
775 hydrates at active seep sites in the eastern Black Sea using pressure coring technique. Biogeosciences 8,
776 3555-3565.
777 Hillman, J.I.T., Klaucke, I., Bialas, J., Feldman, H., Drexler, T., Awwiller, D., Atgin, O., Cifci, G., 2018.
778 Gas migration pathways and slope failures in the Danube Fan, Black Sea. Marine and Petroleum
779 Geology, 92, 1069-1084.
780 Hyndman, R.D., Spence, G.D, 1992. A seismic study of methane hydrate marine bottom simulating
781 reflectors. Journal of Geophysical Research, 97(B5), 6683-6698.
782 Jackson, P.D., Taylor Smith, D., Stanford, P.N., 1978. Resistivity-porosity-particle shape relationships for
783 marine sands. Geophysics, 43(6), 1250-1268.
784 Ker, S., Thomas, Y., Riboulot, V., Sultan, N., Bernard, C., Scalabrin, C., Ion, G., Marsset, B., 2019.
785 Anomalously deep BSR related to a transient state of the gas hydrate system in the western Black Sea.
786 Geochemistry, Geophysics, Geosystems, 20, 442–459.
787 Kessler, J.D., Reeburgh, W.S., Southon, J., Seifert, R., Michaelis, W., Tyler, S.C., 2006. Basin-wide
788 estimates of the input of methane from seeps and clathrates to the Black Sea. Earth and Planetary
789 Science Letters, 243, 366-375.

Journal Pre-proof

790 Key, K., 2016. MARE2DEM: a 2-D inversion code for controlled-source electromagnetic and
791 magnetotelluric data. Geophysical Journal International, 207, 571-588.
792 Klaucke, I., Sahling, H., Weinrebe, R. W., Blinova, V., Bürk, D., Lursmanashvili, N., Bohrmann, G., 2006.
793 Acoustic investigation of cold seeps offshore Georgia, eastern Black Sea. Marine Geology, 231(1-4),
794 51-67.
795 Kruglyakova, R.P., Byakov, Y.A., Kruglyakova, M.V., Chalenko, L.A., Shevtsova, N.T., 2004. Natural oil
796 and gas seeps on the Black Sea floor. Geo-Marine Letters, 3, 150-162.
797 Kvenvolden, K.A., 1993. Gas hydrates—geological perspective and global change. Reviews of Geophysics,
798 31(2), 173-187.
799 Lee, M.W., Collett, T.S., 2006. A Method of Shaly Sand Correction for Estimating Gas Hydrate Saturations
800 Using Downhole Electrical Resistivity Log Data. U.S. Geological Survey Scientific Investigations
801 Report 2006-5121, 10 pages.
802 Lüdmann,T., Wong, H.K., Konerding, P., Zillmer, M., Petersen J., Flüh, E. 2004. Heat flow and quantity of
803 methane deduced from a gas hydrate field in the vicinity of the Dnieper Canyon, northwestern Black
804 Sea. Geo-Marine Letters 24(3), 182-193.
805 Majumdar, U., Cook, A.E., Shedd, W., Frye, M., 2016. The connection between natural gas hydrate and
806 bottom-simulating reflectors. Geophysical Research Letters, 43, 7044–7051.
807 McDougall, T.J., Barker, P.M., 2011. Getting started with TEOS-10 and the Gibbs Seawater (GSW)
808 Oceanographic Toolbox, 28 pages.
809 Milkov, A.V., 2004. Global estimates of hydrate-bound gas in marine sediments: how much is really out
810 there? Earth Science Reviews, 66, 183-197.
811 Minshull, T.A., Marín-Moreno, H., Betlem, P., Bialas, J., Bünz, S., Burwicz, E., Cameselle, A.L., Cifci, G.,
812 Giustiniani, M., Hillman, J.I.T., Hölz, S., Hopper, J.R., Ion, G., León, R., Magalhaes, V., Makovsky, Y.,
813 Mata, M.-P., Max, M.D., Nielsen, T., Okay, S., Ostrovsky, I., O'Neill, N., Pinheiro, L.M., Plaza-
814 Faverola, A.A., Rey, D., Roy, S., Schwalenberg, K., Senger, K., Vadakkepuliyambatta, S., Vasilev, A.,
815 Vázquez, J.-T., 2020. Hydrate occurrence in Europe: a review of available evidence. Marine Petroleum
816 and Geology, 111, 735-764.

817 Murray J. W., Top, Z., Ozsoy, E., 1991. Hydrographic properties and ventilation of the Black Sea. Deep-
818 Sea Research, 38, 663-689.
819 Naudts, L., Greinert, J., Artemov, Y., Staelens, P., Poort, J., Van Rensbergen, P., De Batist, M., 2006.
820 Geological and morphological setting of 2778 methane seeps in the Dnepr paleo-delta, northwestern
821 Black Sea. Marine Geology, 227(3-4), 177-199.
822 Pape, T., Bahr, A., Klapp, S.A., Abegg, F., Bohrmann, G., 2011. High-intensity gas seepage causes rafting
823 of shallow gas hydrates in the southeastern Black Sea. Earth and Planetary Science Letters 307, 35-46.
824 Pearson, C.F., Halleck, P.M., McGuire, P.L., Hermes, R., Mathews, M., 1983. Natural Gas Hydrate
825 Deposits: A Review of insitu properties. Journal of Physical Chemistry, 87, 4180 – 4185.
826 Piñero, E., Marquardt, M., Hensen, C., Haeckel, M., Wallmann, K., 2013. Estimation of the global
827 inventory of methane hydrates in marine sediments using transfer functions. Biogeosciences, 10(2),
828 959–975.
829 Popescu, I., DeBatist, M., Lericolais, G., Nouze, H., Poort, J., Panin, N., Versteeg, W., Gillet, H., 2006.
830 Multiple bottom simulating reflectors in the Black Sea: Potential proxies of past climate conditions.
831 Marine Geology 227, 163-176.
832 Popescu, I., Gilles, L., Panin, N., Batist, M., Herve, G., 2007. Seismic expression of gas and gas hydrates
833 across the western Black Sea. Geo-Marine Letters, 27(2-4), 173-183.
834 Reeburgh, W.S., Ward, B.B., Whalen, S.C., Sandbeck, K.A., Kilpatrickt, K.A., Kerkhof, L.J., 1991. Black
835 Sea methane geochemistry. Deep Sea Research Part A, Oceanographic Research Papers, 38(Suppl. 2),
836 S1189-S1210.
837 Riboulot, V., Cattaneo, A., Scalabrin, C., Gaillot, A., Jouet, G., Ballas, G., Marsset, T., Garziglia S., Ker,
838 S., 2017. Control of the geomorphology and gas hydrate extent on widespread gas emissions offshore
839 Romania. Bulletin De La Société Géologique De France, 188(4), 26–12.
840 Riboulot, V., Ker, S., Sultan, N. Thomas,Y., Marsset, B., Scalabrin, C., Ruffine, L., Boulart, C., Ion, G.,
841 2018. Freshwater lake to salt-water sea causing widespread hydrate dissociation in the Black Sea. Nature
842 Communications, 9,117.

Journal Pre-proof

Riedel, M., Novosel, I., Spence, G.D., Hyndman, R.D., Chapman, R.N., Solem, R.C., Lewis, T., 2006. Geophysical and geochemical signatures associated with gas hydrate–related venting in the northern Cascadia margin. GSA Bulletin, 118 (1-2), 23-38.

Riedel, M., Freudenthal, T., Bergenthal, M., Haeckel, M., Wallmann, K., Spangenberg, E, Bialas, J., Bohrmann, G., 2020. Physical properties, in situ temperature, and core-log seismic integration at the Danube Deep-Sea Fan, Black Sea. Marine and Petroleum Geology, 114, 104192, this issue.

Ruppel, C.D., Kessler, J.D., 2017. The interaction of climate change and methane hydrates. Reviews of Geophysics. 55, 126 – 168.

Salem, H.S., Chilingarian, G.V., 1999. The cementation factor of Archie's equation for shaly sandstone reservoirs. Journal of Petroleum Science and Engineering, 23, 83–93.

Sava D.C., Hardage, B.A., 2007. Gas-hydrate concentration and uncertainty estimation from electrical resistivity logs: examples from Green Canyon, Gulf of Mexico. SEG Technical Program Expanded Abstracts 2007, 4 pages.

Schmale, O., Haeckel, M., McGinnis, D. F.,2011. Response of the Black Sea methane budget to massive short-term submarine inputs of methane. Biogeosciences 8, 911-918.

Schwalenberg, K., Rath, V., Haak, V., 2002. Sensitivity studies applied to a two-dimensional resistivity model from the Central Andes. Geophysical Journal International, 150, 673-686.

Schwalenberg, K., and Scientific Party of MSM 35, 2014. SUGAR SITE - CSEM, Cruise MSM35, January 20 – February 5, 2014, Varna (Bulgaria) – Istanbul (Turkey), MARIA S. MERIAN Berichte, Bremen, 49 pages.

Schwalenberg, K., Rippe, D., Koch, S., Scholl, C., 2017. Marine□controlled source electromagnetic study of methane seeps and gas hydrates at Opouawe Bank, Hikurangi Margin, New Zealand, Journal of Geophysical Research, Solid Earth, 122, 3334 – 3350.

Simandoux, P., 1963. Dielectric measurements in porous media and application to shaly formation. Revue de L'Institut Français du Pétrole, 18, Supplementary Issue, 193–215.

Sloan, E.D., Koh, C., 2007. Clathrate Hydrates of Natural Gases, CRC press, Boca Raton, Fla., 752 pages

Journal Pre-proof

Journal Pre-proof

869 Soulet, G., Delaygue, G., Vallet-Coulomb, C., Böttcher, M., Sonzogni, C., Lericolais, G., Bard, E., 2010.
870 Glacial hydrologic conditions in the Black Sea reconstructed using geochemical pore water profiles.
871 Earth and Planetary Science Letters, 296(1-2), 57-66.
872 Spangenberg, E., 2001. Modeling of the influence of gas hydrate content on the electrical properties of
873 porous sediments. Journal of Geophysical Research, 106, 6535-6548.
874 Tréhu, A.M., Bohrmann, G., Torres, M.E., and Colwell, F.S. (Eds.), 2006. Proceeding ODP, Scientific
875 Results, 204, College Station, TX (Ocean Drilling Program).
876 Vassilev, A., Dimitrov, L.I., 2002. Spatial and quantity evaluation of the Black Sea gas hydrates, Russian
877 Geology and Geophysics 43, 672-684.
878 Vassilev, A., 2005. Gas Hydrates as Sources of Huge Methane Seepages (Case Study: Paleo-Dnepr &
879 Dvurechenskii , Black Sea). Geophysical Research Abstracts, 7., 04613.
880 Wallmann, K., Bialas, J., 2009. SUGAR -submarine gas hydrate reservoirs. Environmental Earth Sciences,
881 59(2), 485-487.
882 Weitemeyer, K., Constable, S., Shelander, D., Haines, S., 2017. Mapping the resistivity structure of Walker
883 Ridge 313 in the Gulf of Mexico using the marine CSEM method. Marine and Petroleum Geology, 88,
884 1013-1031.
885 Winsauer, W.O., Shearin, H.M., Masson, P.H., Williams, M., 1952. Resistivity of Brine Saturated Sands in
886 relation to Pore Geometry. American Association of Petroleum Geologists Bulletin, 36(2), 253- 277.
887 Worthington, P.F., 1993. The uses and abuses of the Archie equations, 1: The formation factor-porosity
888 relationship. Journal of Applied Geophysics, 30, 215-228.
889 Zander, T., Haeckel, M., Berndt, C., Chi, W.C., Klaucke, I., Bialas, J., Klaeschen, D., Koch, S., Atgin, O.,
890 2017. On the origin of multiple BSRs in the Danube deep-sea fan, Black Sea. . Earth and Planetary
891 Science Letters, 462, 15–25.
892 Zander, T., Choi, J.C., Vanneste, M., Berndt, C., Dannowski, A., Carlton, B., Bialas, J., 2018. Potential
893 impacts of gas hydrate exploitation on slope stability in the Danube deep-sea fan, Black Sea. Marine and
894 Petroleum Geology, 92, 1056-1068.

Journal Pre-proof

Highlights

- First 2D CSEM study on Black Sea gas hydrates
- Joint Interpretation of marine CSEM, seismic and drilling data
- Stochastic determination of gas hydrate saturation estimates

Journal Pre-proof

Journal Pre-proof

Declaration of interests

☒ The authors declare that they have no known competing financial interests or personal relationships that could have appeared to influence the work reported in this paper.

☐The authors declare the following financial interests/personal relationships which may be considered as potential competing interests:

Journal Pre-proof